International Journal of Multiphase Flow 178 (2024) 104886

Contents lists available at ScienceDirect

International Journal of Multiphase Flow

journal homepage: www.elsevier.com/locate/ijmulflow

Porous structures impact on particle dynamics of non-Brownian and noncolloidal suspensions

Eileen A. Haffner[a], Theresa Wilkie[a], Jonathan E. Higham[b], Parisa Mirbod[a,*]

[a] *Department of Mechanical and Industrial Engineering, University of Illinois at Chicago, 842 W. Taylor Street, Chicago, IL 60607, USA*
[b] *School of Environmental Sciences, University of Liverpool, Liverpool, UK*

ARTICLE INFO

Keywords:
Porous structures
Particle Image velocimetry
Very dilute suspensions
Particle focusing
Optical flow tracking velocimetry
Low Reynolds number flows

ABSTRACT

This study aims to provide valuable insights into the impact of porous structures on particle dynamics in non-Brownian, non-colloidal suspension flows at very low Reynolds numbers. Two experimental approaches, Particle Image Velocimetry (PIV) with refractive index matching and Optical Flow Tracking Velocimetry (OFTV) were employed to analyze very dilute suspensions over various porous media models. The study considered three different porous structures with permeabilities ranging from 0.7 to 0.9 and three different thicknesses ranging from 0.2 cm to 0.5 cm, while the suspension bulk volume fraction was maintained at 3 %. In the PIV analysis, we observed that decreasing the porous permeability resulted in the maximum velocity location within the free flow region moving closer towards the interface between the flow and the porous media. We further quantified the effect of the porous structure on the suspension by characterizing interface properties, such as dimensionless slip velocity, shear rate, and slip length. These interface properties were found to be influenced by both the thickness and permeability of the porous media. Next, we analyzed particle migration due to the presence of porous structures using OFTV for very dilute suspensions of 1 %, 2 %, and 3 %, considering a porous medium with known physical properties and thickness. The study revealed two local concentration maxima: one within the free flow region on top of the rod arrays used to create the porous structure and a second along the rods' centerline inside the porous media model.

1. Introduction

Suspensions in low Reynolds number flows are common in technological and industrial applications such as biological and biomedical devices, microfluidics, extrusion, food processing, and manufacturing (Barnes, 1981; Larson, 1999; van Dinther et al., 2012). Defined as regions with both solid structure and void space, porous media have also been observed in various natural scenarios, from sediment on stream beds to the airflow over bird feathers. Minimizing energy loss and inefficiencies in these technologies require the application of effective control and poses a substantial challenge. Such control and driving of the fluid flow rely on maintaining proper boundary conditions in these systems. Several experimental techniques have been developed to study flows containing particles (suspension flows) in smooth pressure-driven and simple shear flows, covering the range from creeping flow to turbulent regimes. Despite these studies, the complex interactions between low Reynolds number flow dynamics and particle behavior within porous media remains poorly understood.

Previous experiments in higher Reynolds number flows in porous media have identified two-dimensional (2D) velocity fields, indicating the effect of inertia and drag, which are proportional to the pore size (Johnston et al., 1975). Laser Doppler velocimetry (LDV) studies have led to the discovery of a jet-like structure within the pores at higher Reynolds numbers (Hall and Hiatt, 1994). Particle image velocimetry (PIV) in conjunction with refractive index matching (RIM) techniques has been applied to various porous media applications, including the study of flow within the pores of a porous media, specifically pressure-driven flow through packed beads (Peurrung et al., 1995; Patil and Liburdy, 2013). Another unique flow field in porous media is created when the media is bounded by a free-flow region above it, more closely representing porous media flows in real-world settings. The flow physics of suspensions in various applications has received much attention; see (Morris, 2020) for a review.

At lower Reynolds numbers, prior studies using laser Doppler anemometry (LDA) (Jana et al., 1995; Koh et al., 1994; Kapoor and Acrivos, 1995) or LDV (Averbakh et al., 1997; Lyon and Leal, 1998a,

---

* Corresponding author.
E-mail address: pmirbod@uic.edu (P. Mirbod).

https://doi.org/10.1016/j.ijmultiphaseflow.2024.104886
Received 24 October 2023; Received in revised form 4 May 2024; Accepted 31 May 2024

1998b) with RIM techniques have explored particle volume fractions ranging from 10 % to 50 % with corresponding particle and flow Reynolds numbers of $Re_p = O(10^{-3})$ to $O(10^{-6})$ and $Re \leq 1$, respectively. These techniques effectively detect velocity vectors and related concentration fields. A critical observation from these studies is that suspension particles tend to migrate to paths of least resistance within the channel center, leading to a local increase in concentration along the channel centerline and causing a blunted velocity profile at the mid-center for high particle volume fractions (Lyon and Leal, 1998a; Koh et al., 1994; Kapoor and Acrivos, 1995; Averbakh et al., 1997; Lyon and Leal, 1998b).

In low Reynolds number Couette flows, PIV has been applied to study wall-slip phenomena where the presence of particles causes a slip velocity at the solid, impermeable boundary of the channel (Jesinghausen et al., 2016). PIV has also been used to observe the blunted velocity profiles for particle solid volume fractions ranging from 20 % to 50 % (Singh et al., 2006). For higher Reynolds numbers, PIV has been applied to study particle migrations in rectangular channels (Zade et al., 2018; Miura et al., 2014). The discussed studies primarily utilized LDV and LDA for non-Brownian suspensions, characterized by a large Pélect number (*Pe*). However, PIV has also been applied to investigate Brownian suspensions in pressure-driven flows at particle volume fractions ranging from 0.05 to 0.34, focusing on the effect of Pélect number ($47 \leq Pe \leq 500$) on the flow structure (Frank et al., 2003; Semwogerere et al., 2007).

Magnetic resonance imaging (MRI) or nuclear magnetic resonance imaging (NMRI) has also been used to investigate suspension flows in various configurations. Similar to LDA and LDV, MRI experiments enable the measurement of velocity and concentration within a three-dimensional (3D) space. Pressure-driven suspension flows through pipes (Sinton and Chow, 1991; Hampton et al., 1997) have been investigated using MRI. This technique has also been applied to bifurcating channels on both macro and microscales in a low Reynolds number regime (Xi and Shapley, 2008; Roberts and Olbricht, 2006). Our recent examinations of suspensions ranging from 10 % to 40 % particle volume fraction using MRI over a porous structure have revealed modification in the velocity profiles and heterogeneous concentration fields for various suspensions (Mirbod and Shapley, 2023). While MRI offers advantages beyond those of widely used optical techniques, such as LDA, LDV, and PIV, namely, the ability to obtain particle concentration data and access optically opaque systems, it has drawbacks. For example, particle tracking cannot be performed in MRI since the image pixels are likely to be larger than the pore size.

The present study uses PIV and optical flow tracking velocimetry (OFTV) to characterize very dilute suspension flows within porous media models and presents quantitative evidence and new insights into the behavior of very dilute suspensions flowing over and through porous media models with varying properties (e.g., permeability and porosity) and thickness. Additionally, the study sheds light on particle migration due to the presence of porous structures in a very dilute regime. Previous work from our group has focused on isolating the flow physics of very dilute suspensions over a specific porous medium by presenting only velocity profiles (Haffner and Mirbod, 2020) or understanding semi-dilute suspensions with bulk volume fractions ranging from 10 % to 40 % over a specific porous media model (Mirbod and Shapley, 2023). In this study, we first explore a very dilute suspension with a particle volume fraction of $\phi_b = 3$ % over various porous media models with known physical properties and different thicknesses. Our objective is then first to examine how the properties of the porous structure affect the velocity profile and flow interface characteristics (e.g., slip velocity, shear rate, and slip length). Next, we analyze particle migration over and through a porous medium model with porosity $\varepsilon = 0.9$, permeability $K = 7.92 \times 10^{-3}$ cm^2, and thickness $H = 0.5$ cm for three different very dilute suspensions (i.e., $\phi_b = 1$ %, $\phi_b = 3$ %, $\phi_b = 5$ %). The particle to pore size ratio ranges from 0.78 to 0.52. We employ PIV with RIM and OFTV to provide insights into the behavior of suspensions at very low Reynolds numbers (where inertia is neglected). The obtained measurements of particle concentration and velocity distributions provide key information leading to a deeper understanding of the suspension flows and particle motion over and inside various porous structures.

In the following, the experimental setup is described in Section 2, the results are presented and discussed in Section 3, and concluding remarks are presented in Section 4.

2. Experimental procedure

2.1. PIV apparatus and acquisition

Our study utilized the Particle Image Velocimetry (PIV) technique to visualize, depict, and record velocity regimes of suspensions flowing over and through a channel partially obstructed by various porous media models. The PIV experiments were conducted to obtain velocity information in both the free flow region and within the porous media. Detailed procedures for the PIV can be found in our previous work (Haffner and Mirbod, 2020) and the relevant literature (Raffel et al., 2018; Adrian and Westerweel, 2011). The experimental techniques employed in this study encompass both suspensions (Jesinghausen et al., 2016; Ramesh et al., 2019) and porous media (Arthur et al., 2009; Haffner and Mirbod, 2020). For these experiments, we utilized a LaVision FlowMaster particle image velocimetry system, which includes a 527 nm Nd-YLF laser (Photonics Industries, DM20-527) to illuminate fluorescent seeding particles with diameters ranging from 1 to 5 μm and a density of 1300 kg/m^3 in the test section. The fluorescence exhibited by these seeding particles has a peak excitation at 594 nm and peak emission at 460 nm. To capture the images, a 550 nm broadpass filter and a Micro Lab 320 high-speed camera (Phantom, Vision Research Inc.) were employed. The PIV experimental setup is depicted in Fig. 1(a). Laser sheet optics were used to spread the laser beam into a 1 mm thick sheet, which was then vertically directed into the test section of the channel using a 2.54 cm diameter mirror (Edmund Optics). The seeding particles were illuminated as they moved through the laser sheet, and a series of images were captured at a specified frequency. The DaVis 10.0.5 software (LaVision, Inc.) utilized a cross-correlation function to determine the particle location and the particle shift from image to image. The software then calculated the distance traveled by the particles, which was then divided by the time between respective images to determine the velocity (Raffel et al., 2018; Adrian and Westerweel, 2011). The physical parameters for the flow channel are outlined in (Haffner and Mirbod, 2020).

Due to the three-dimensional (3D) structure of the porous media model, two different PIV data collection planes were considered: P$_1$, placed in between the rods, and P$_2$, placed on top of the rods. In our prior work, we determined that these two planes are necessary to fully resolve the flow field over the porous media (Arthur, 2019; Arthur et al.,2009; Haffner and Mirbod, 2020) in the same channel. For collecting the raw PIV images, we found that a sample size of 3000 images was sufficient to fully resolve the flow field. Fig. 1(d) and (e) show examples of the raw PIV images for the P$_1$ and P$_2$ data collection planes, respectively (Haffner and Mirbod, 2020). This data was collected at a frequency of 250 Hz with a laser current of 20 amps. The raw PIV images have a field of view (FOV) of 1920 × 1200 pixels^2, resulting in a FOV of approximately 2.2 × 1.4 cm^2. Note that in all figures and analysis herein, the coordinate system starts at the top of the rods, i.e., $y = 0$ is located at the porous model interface. However, for all the raw images shown in Figs. 1(e), (d), and Fig. 3, $y = 0$ starts at the bottom of rods to keep it the same as what we obtained from Davis software.

The raw PIV particle images underwent segmentation into smaller regions known as interrogation windows (IW). Velocity vectors were then computed using a multi-pass approach on these particle images. Initially, a square 64 × 64 pixel IW with a 50 % overlap was utilized. The IW overlap method was employed to mitigate PIV error linked with

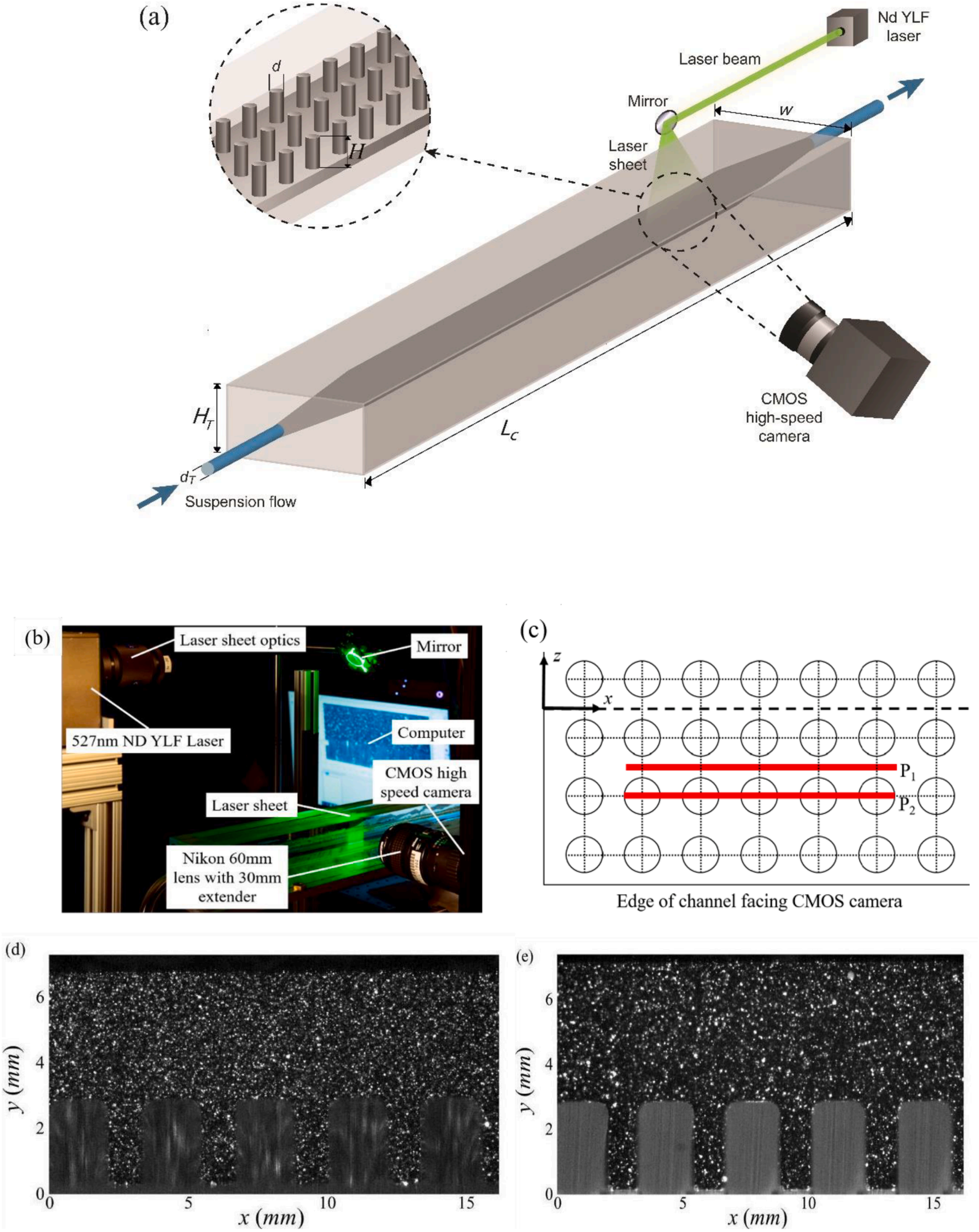

Fig. 1. (a, b) A schematic of the channel and the experimental PIV setup used to map velocity vectors throughout the field of view (Haffner and Mirbod, 2020). (c) The location of the two data collection planes within the porous medium. In the diagram, H is the porous media thickness and d is the diameter of the porous media rods, these values are summarized in Table 1. The external dimensions of the experimental channel, $H_T = 0.72$ cm, $w = 2.54$ cm and $L_C = 100$ cm. Samples of raw particle images captured for characterizing the flow patterns from the (d) P_1 plane and the (e) P_2 plane using PIV. The coordinate system i.e., $y = 0$ locates at the porous medium interface.

particle loss, which occurs when particles exit IWs. Following the initial pass, four additional passes were conducted using circular IWs of either 36×36 pixel^2 or 24×24 pixel^2, depending on the desired density of velocity vectors within the image region. This approach yielded velocity vectors spaced approximately every 0.07 mm or 0.12 mm for a 24×24 pixel^2 IW or 36×36 pixel^2 IW, respectively. As a result, this technique incurred an associated error of roughly 3.24 % of the maximum velocity. We determined this uncertainty using methods summarized by

(Coleman and Steele, 1995; Sciacchitano and Wieneke, 2016), based on the velocity standard deviation and the vector spacing. These PIV images were then processed using the DaVis 10.0.5 software (LaVision, Inc.), following the same approach outlined in (Haffner and Mirbod, 2020). For further details regarding the PIV methodology including outlier detection, overlap of interrogation areas and average pixel displacement we followed the procedure outlined in Raffel et al. (2018); Adrian and Westerweel (2011); Wiederseiner et al. (2011); Westerweel et al. (2013); Hinsch et al. (1993).

2.2. Suspensions, working fluids, and data analysis

The PIV is an optical experimental technique that requires refractive index matching (RIM) to accurately visualize the suspension. To achieve this, our solution matched both the refractive index and the suspension particle's density to make them neutrally buoyant, ensuring that their motion solely depends on the fluid. The solvent consisted of 55 % wt Trition X-100 (Sigma-Aldrich), 25 wt.% 1,6-dibromohexane (Sigma-Aldrich), 10 wt.% UCON oil 75-H-450 (Dow Chemical Company), and 10 wt.% UCON oil 75-H-90000 (Dow Chemical Company). This stable solution has a similar index of refraction to that of the suspension particles.

For our study, we selected polymethyl methacrylate (PMMA) particles with monodispersed diameters, d_p between 75 μm and 90 μm and a mean diameter of 82 μm (Cospheric, LLC), with a density of 1200 $\frac{\text{kg}}{\text{m}^3}$. The bulk suspension volume fraction for all the experiments examining the porous structure properties were kept constant at 3 %. Additional OFTV experiments utilized suspensions with total bulk concentrations of 1 %, 2 %, and 3 %. The bulk particle solid volume fraction (ϕ_b) was 3 % and it was calculated using the formula $\phi_b = \frac{\pi d_p^3 N}{6 V_{\text{total}}}$, where d_p is the average diameter of the suspension particles, N is the total number of particles within the suspension, and V_{total} is the volume of the flow channel. The suspension was mixed for 1 h to ensure proper mixing of the fluid components, and it was placed in a vacuum chamber to remove any bubbles. While particles have a slightly lower density than the suspended fluid, after a long time of rest, such as overnight, any particle settling during the experiment was minimized by mixing the inlet reservoir and applying shearing motion, both known to promote resuspension (Tripathi and Acrivos, 1999). The preparation of the solvent is detailed in our previous publication (Haffner and Mirbod, 2020).

We implemented these protocols to monitor temperature during our experiments. To ensure accurate results, we maintained a transparent suspension with particle concentrations below 3 %, given the experiments' high sensitivity to temperature and humidity fluctuations. Consequently, a careful refractive index matching (RIM) procedure was essential for dependable measurements in particle suspensions. It is noteworthy that optical visualization techniques, including both PIV and OFTV utilized in this study, encountered several challenges in achieving optimal visibility. These challenges included variations in the index of refraction among particles due to manufacturing processes, impurities in the particles or fluid (such as gas bubbles) hindering visibility, and temperature gradients within the suspension affecting visibility. Therefore, the selection of particles with superior optical properties—such as a consistent index of refraction and minimal impurities—was vital. We even observed that using particles of inferior quality resulted in an opaque particle suspension despite our efforts to match the fluid and control temperature diligently.

While we did not have access to construct a temperature-controlled water bath in our setup, our channel was temperature-controlled using two water-cooled bath next to its sidewalls. Thermometers were employed in the water bath and suspension reservoir, and the flow rate and temperature were also controlled in real-time by a flowmeter (mini CORI-FLOW, Bronkhorst USA) positioned between the end of the dampener and the start of the flow channel. This ensured a constant temperature of 22 °C to maintain the refractive index, density, and viscosity of the flow during the experiment while the flow Reynolds number was kept very low. To determine the new mixture, we measured the density of each fluid using a hydrometer and the index of refraction using a refractometer (Cole–Parmer), both at ambient laboratory temperature. These measurements allowed us to determine the necessary concentration for the PMMA particles we used and the ambient temperature during the experiments. Also, we conducted multiple tests while continuously monitoring temperature and humidity to ensure that these factors did not affect our experimental data.

The viscosity of both the suspending fluid and suspensions have been determined using a concentric cylinder rheometer (Discovery Hybrid Rheometer-2, TA Instruments Inc.). They exhibited a Newtonian response over a wide range of shear rates, with a viscosity of 0.288 Pa s at 22 °C. Also, in all tests we ensured that the measured temperature dependence of the suspending fluid's refractive index and density required the lab temperature to remain within ±1 °C, following prior works reported by Lyon and Leal (1998b); Koh et al. (1994). As a result, due to our use of highly diluted suspension flows (1 %, 2 %, and 3 % by volume), we noted only minimal temperature fluctuations. However, we recognized that temperature regulation become increasingly critical with higher suspension concentrations.

The complexity of our experimental setup requires consideration of multiple dimensionless parameters, including the Reynolds number, the Stokes number, and the Pélect number. We examine three different Reynolds numbers in our experiments, each describing how the flow moves through various aspects of our setup. The particle Reynolds number is calculated using an equation defined by Lyon and Leal (1998a, 1998b), $Re_p = \frac{4 p_f a^3}{3 \mu_f L^2} |U_{\max}|$. Here ρ_f is the density of the fluid, μ_f is the viscosity of the Newtonian fluid, L is half height of the free flow region ($2L = H_T - H$), a is the average radius of the suspension particles, ρ_f is the density of the solvent fluid, and $U_{\max}$ is the maximum velocity in the streamwise direction. The particle Reynolds number is computed to be very small, $Re_p \sim O(10^{-6})$, allowing the inertial effects on the particles to be neglected. The porous Reynolds number describes how the suspension moves through the porous medium. This equation is $Re_L = \frac{p_f d U_b}{\mu(\phi_b)}$, where d is the diameter of the rods in the porous medium, U_b is the bulk velocity ($U_b = \frac{1}{H_T} \int_{-H}^{2L} u(y) dy$) in the streamwise direction, and $\mu(\phi_b)$ is the Krieger viscosity (Krieger, 1972) defined as $\mu(\phi_b) = \mu_f \left(1 - \frac{\phi_b}{\phi_m}\right)^{-\beta}$ where ϕ_m is the maximum packing particle solid volume fraction and β is a rheological fitting parameter. It is important to acknowledge that while experiments have determined the densest random packing of monodisperse spheres to occur near 0.64 (Bernal and Mason, 1960), in practical applications, the packing fraction can vary based on the degree of polydispersity. For instance, it may increase from 0.64 for monodisperse packings to approximately 0.75 for packings with 0.65 polydispersity (Sohn and Moreland, 1968). Researchers have numerically observed that both polydispersity and skewness influence the maximum random close packing volume fraction (Desmond and Weeks, 2014). Our findings indicate that the Maximum packing fraction depends on various factors such as particle size distribution, roughness and the interaction of particles, suspension type (Brownian or non-Brownian), and particle concentration. In our study, we then considered $\beta = 2$ and $\phi_m = 0.68$ as reported in Miller and Morris (2006); however, since ϕ_b is very dilute in our case, variation in ϕ_m are not expected to significantly affect $\mu(\phi_b)$.

The last Reynolds number to consider is the suspension Reynolds number, which depicts how the suspension fluid moves, as whole, through the test section. Mathematically, this is defined as $Re_S = \frac{p_f L U_b}{\mu(\phi_b)}$. For our purposes, the fluid regime was kept and calculated in the creeping flow regime so $Re_S < 0.1$. The values for all these Reynolds numbers are summarized for the various test cases in Table 1. The Stokes number is used to determine if the particle inertial forces are critical (Miller and Morris, 2006; Ramesh et al., 2019). The Stokes number was computed and defined to be low, $St \sim O(10^{-5})$. The Pélect number is used to determine if molecular forces would affect the motion of the suspension particles. The Pélect number is very large for the range of shear rate used in our experiments, $O(10^9)$, which makes the suspension non-Brownian, so the intermolecular forces are negligible. These dimensionless parameters are controlled in this way so that the suspension particles react quickly to changes in the flow field. We also showed in our previous work that the flow over and through a porous media has both streamwise and spanwise components of velocity (Haffner and Mirbod, 2020). Accordingly, the magnitude of the velocity seen in Table 1 was calculated by $U(y) = \sqrt{u(y)^2 + v(y)^2}$. The resulting bulk velocity can then be defined over the y direction by $U_b = \frac{1}{H_T}\int_{-H}^{2L} U(y)$.

Different porous media models were made with a high-quality preset in glossy printing mode with a Stratasys Object 30Prime 3D printer (Stratasys). The parameters of the various porous media models are listed in Table 1. The dimensionless parameters related to the porous media are the depth ratio, $\delta = H/L$, and the permeability parameter, $\sigma = L/\sqrt{K}$. Previous literature reported a filling fraction which is the inverse of the depth ratio (James and Davis, 2001; Agelinchaab et al., 2006). The permeability of the porous media is dependent on the porosity, ε, for rigid rods in a square array (Tamayol and Bahrami, 2011). The spacing between the rods was changing between 0.27 cm to 0.15 cm to ensure there are enough particles within the rods; thus, clogging does not arise. We also indicate that to ensure there are enough particles across the gap, the ratio of the particle diameter and the channel gap is very small (≈ 0.012); therefore, the suspension can be considered as a continuum medium. The external dimensions of the experimental channel are $H_T = 0.72$ cm, $w = 2.54$ cm and $L_C = 100$ cm. Note that the coordinate system, i.e., $y = 0$ starts at the porous model interface.

We took specific measures to ensure an adequate distribution of particles across the channel gap. To achieve this, we carefully designed the ratio of the particle diameter to the channel gap to be very small. This choice was made to ensure that the particles are distributed uniformly across the flow, enabling us to treat the suspension as a continuum medium. Treating the suspension as a continuum medium allows us to simplify the analysis, considering the suspension as a continuous fluid rather than individual discrete particles. Moreover, we checked to ensure that the ratio of the gap width to the length of the channel adhered to the guidelines proposed by Lyon and Leal (1998a; Nott and Brady (1994); Lyon and Leal (1998b). These guidelines are essential to ensure that the particles within the suspension reach a fully developed region. A fully developed region refers to a section of the flow where the velocity profile remains constant along the flow direction, and any changes in the flow are negligible. For our experiments with a 40 % particle concentration, we estimated that the fully developed length in the smooth region is approximately 10 m. However, it is important to acknowledge that during our measurements, the suspension flow may still be in the process of developing, meaning that the velocity profiles might not have fully reached a fully developed state. Additionally, the presence of the 3D geometry of the porous media used in our study results in a three-dimensional suspension flow inside the channel. As a result, we conducted a detailed examination of the fully developed flow for our proposed porous model. This investigation allowed us to gain a deeper understanding of the behavior of the suspension within the channel and how the 3D structure of the porous media influences the flow dynamics.

2.3. Flow stability analysis

To assess the stability of the flow for fully developed velocity profiles over and through the porous media models, we analyzed velocity vectors along the x axis below the interface. The porous media models, measuring 28.4 cm in length, are positioned at a distance of 8 cm from the channel inlet. To conduct this analysis, we obtained different fields of view (FOVs) at intervals of 1cm along the channel. These FOVs are depicted as red boxes in Fig. 2(a). The first FOV corresponds to the start of the porous media, and the last FOV is positioned 35 cm from the inlet of the channel (27 cm from the beginning of the porous media). In Fig. 2 (b–d), we present the streamwise velocity at a dimensionless height of $\frac{y}{L} = -0.12$ for both data collection planes, considering a thickness of $H = 5$ mm. Similarly, Fig. 2(e–g) illustrates the streamwise velocity for $H = 2$ mm. The blue dots and the red dots show the streamwise velocity over the entire porous media for both data collections planes, P_1 and P_2. As observed in the figures, non-zero u-component velocities are evident in the regions between the rods of the porous media, while the velocity values become zero at the physical locations of the rods. This analysis provides insights into the flow behavior within and around the porous media models, highlighting the impact of the porous structure on the velocity distribution.

The stable Fields of View (FOVs) are identified by black boxes for both the P_1 and P_2 data collection planes. In Fig. 2(e–g), we present the stability characterization for the porous media thickness $H = 2$ mm ($\delta = 0.74$) and different permeabilities. For Fig. 2(e, f), the flow does not exhibit periodic behavior until reaching a point 29 cm downstream from the channel inlet and 21 cm from the start of the porous media. Note that although we conducted each test three times, and also implemented camera calibration to ensure its alignment perpendicular to the measurement plane, we continue to observe a pronounced trend in velocity in Fig. 2(f) which might be due to the structure of the porous media model for the specific values of $\delta = 0.74$ and $\sigma = 3.46$. In the case of $\sigma = 2.2$, shown in Fig. 2(g), the flow becomes periodic at 26 cm, which is further upstream compared to the other two permeabilities. Our observations indicate that both dimensionless parameters, the depth ratio δ, and the permeability parameter σ, significantly impact the flow stability over the porous media models. Higher depth ratios result in a stable flow further upstream along the porous media compared to the cases with lower depth ratios. Conversely, porous media with the lowest permeability parameter exhibits a similar effect, where the flow reaches

Table 1
Experimental parameters for various porous media models examined in this study.

K (cm^2)	ε	σ	d (cm)	H (cm)	$2L$ (cm)	δ	U_b (cm/s)	Re_p	Re_L	Re_S
1.12×10^{-3}	0.7	6.09	0.2	0.2	0.51	0.74	0.76	7.92×10^{-7}	0.057	0.077
				0.3	0.41	1.37	0.71	9.72×10^{-6}	0.054	0.062
				0.5	0.21	4.54	0.65	7.42×10^{-6}	0.044	0.032
3.42×10^{-3}	0.8	3.46	0.2	0.2	0.51	0.74	0.77	6.49×10^{-7}	0.057	0.081
				0.3	0.41	1.37	0.75	1.34×10^{-6}	0.056	0.058
				0.5	0.21	4.54	0.64	3.96×10^{-6}	0.048	0.026
7.92×10^{-3}	0.9	2.2	0.15	0.2	0.51	0.74	0.81	7.63×10^{-7}	0.061	0.079
				0.3	0.41	1.37	0.77	1.12×10^{-6}	0.044	0.062
				0.5	0.21	4.54	0.79	4.69×10^{-6}	0.059	0.035

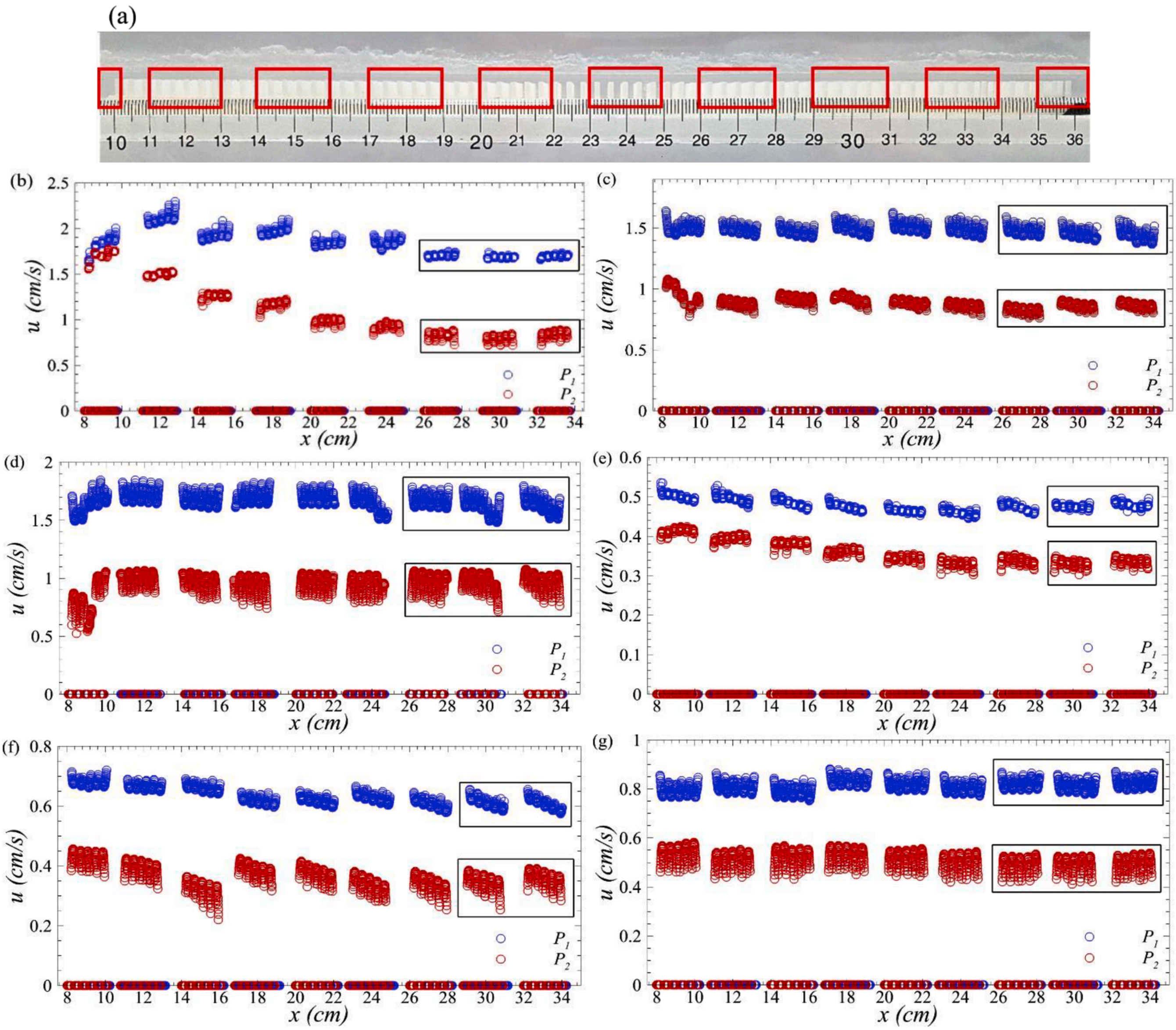

Fig. 2. (a) The side view of the flow channel containing the porous media. The red boxes show the location of each FOV along the length of the porous media in the x axis. The streamwise velocity at $y\_ = -0.12$ (a L point below the physical interface between the porous media and the free flow region) for $H = 5$ mm ($\delta = 4.54$) (b) $K = 1.12 \times 10^{-3}$ cm^2($\sigma = 6.09$), (c) $K = 3.42 \times 10^{-3}$ cm^2($\sigma = 3.46$), and (d) $K = 7.92 \times 10^{-3}$ cm^2($\sigma = 2.2$). The stability evaluation for the cases $\delta = 0.74$ for (e) $\sigma = 6.09$, (f) $\sigma = 3.46$, and (g) $\sigma = 2.2$. The blue dots and the red dots show the streamwise velocity over the entire porous media for both data collections planes, P_1 and P_2.

a point of periodicity further upstream. In our analysis, we present results based on the FOVs where the flow is fully developed. To determine the fully developed velocity profile describing the motion of the suspension over and through the specific porous media, we calculate an average of the velocity data obtained from the stable FOVs. This approach allows us to accurately characterize the velocity distribution within and over porous structures and to further examine the impact of suspension flows. Prior to conducting experiments with a porous media model, we conducted an initial examination of suspension flow in a smooth channel. This was done to precisely determine the location where the porous slides should be positioned to ensure that the flow is fully developed before encountering the porous media. To accomplish this, we performed a test using a suspension with a bulk concentration of $\phi_b = 0.03$ in a smooth channel where no porous media were present.

The objective was to confirm that the flow had reached full development before reaching the beginning of the porous media. For further details, refer to Fig. 2 in Haffner and Mirbod (2020).

2.4. *Particle volume fraction analysis*

To measure the particle volume fraction profiles, we employed an optical experimental technique called optical flow tracking velocimetry (OFTV). Further details regarding this method, including the related postprocessing and analysis, can be found in our recent publications (Mirbod et al., 2021; Haffner et al., 2021). For these experiments, a portion of the suspension particles was replaced with fluorescent particles having the same diameter range ($75\ \mu\text{m} \le d_p \le 90\mu$) and density ($\rho_p = 1200 \frac{\text{kg}}{\text{m}^3}$) as the PMMA particles used in the PIV experiment. By ensuring that the fluorescent particles have parameters (diameter and density) equivalent to the PMMA particles, we can ensure that the flow physics affecting both particles are identical. Consequently, we assume that all the dimensionless parameters, such as Reynolds numbers, Pélect number, and Stokes numbers remain the same as in the PIV experiments discussed earlier. The fluorescent particles used in the OFTV experiments emit light at a peak wavelength of 607 nm when excited at 575 nm. Due to their high emission, we incorporated two transmission filters (50 % and 79 % transmission) from Edmond Optics in addition to the 550nm broad pass filter used previously. These measurements help enhance the accuracy and sensitivity of the fluorescent particle tracking during the OFTV experiments.

The fluid used in the experiment has the same index of refraction as the PMMA suspension particles. However, due to the large size of the fluorescent particles, the flow becomes less visible. To overcome this challenge and accurately track and characterize the particles in the suspension, we conducted several tests. Based on our findings, we replaced approximately 1/8 of 1 % of the total suspension particles with the fluorescent particles. This resulted in a concentration of 0.12 % fluorescent particles within the suspension. The remaining particles in the suspension were PMMA particles. A threshold for fluorescent intensity was determined based on the maximum intensity observed in the raw images. This threshold aimed to exclude particles partially within the laser sheet, as they would fluoresce less intensely compared to particles fully within the sheet. A Gaussian distribution of fluorescence intensity was applied to individual particles where high fluorescence was detected in the image. The size of the Gaussian distribution was chosen to be 8 pixels based on the image resolution. However, it is important to note that this OFTV technique solely offers particle distribution information in the form of a particle/pixel field map. We conducted three series of experiments, capturing a total of 6000 images in each series, to track the particles in the flow and to explore their migration over and through the porous structure. Fig. 3(a–c) illustrates an example of the raw image obtained for the 1 % suspension flow, where 1/8 of the particles were fluorescent. The images correspond to the P_1 and P_2 data collection planes, as well as the smooth channel, respectively.

To identify and track the PMMA particles in the suspension, we utilized our in-house software, the so-called FlowOnTheGo (Mirbod et al., 2021). This software employs Eigenfeatures to detect particles and verify them based on size, circularity, and inertia thresholds. By solving the optical flow equations using Lucas–Kanade solutions, we determine the particle paths and individual tracks throughout their trajectories. Since the experiments involve a 3D setup with 2D measurements, it is not always possible to track particles across the entire domain. Therefore, we focus on reporting particle velocities where the number of tracked particles is sufficient to reduce statistical uncertainty to less than 1 % (Coleman and Steele, 1995; Sciacchitano and Wieneke, 2016). The methods for particle detection and tracking are consistent with those described in our previous works (Mirbod et al., 2021; Haffner et al., 2021). To obtain particle velocity profiles, we track the centroids of the particles between successive image pairs in the time-resolved recordings. The tracks are first smoothed using convolution with a three-point Gaussian kernel, and then the streamwise and wall-normal components are differentiated with respect to time. It should be noted that this method may encounter challenges when a particle disappears from one frame to another, typically due to moving out of the laser sheet. Therefore, in this study we only report particle velocities where the number of tracked particles is sufficient to reduce statistical uncertainty to less than 1 % (Coleman and Steele, 1995; Sciacchitano and Wieneke, 2016).

3. Results and discussions

3.1. Velocity contours for a suspension over and through various porous media model

In our previous work (Haffner and Mirbod 2020), we investigated the influence of suspension concentration on fluid velocity through a porous media model with $\delta = 4.54$, $\sigma = 2.2$, and three different very dilute suspensions. In this study, we specifically aim to first isolate the effects of changes in porous media properties and thicknesses on the flow. We then selected three different permeabilities and three different thicknesses for the porous media, as summarized in Table 1. Fig. 4 presents the streamwise and transverse fluid velocity contours obtained from the P_1 and P_2 data collection planes. These contours provide a visual representation of the fluid velocity distribution in the experimental setup.

Fig. 4(a–d) show the streamwise fluid velocity contours for two different porous media models with varying porous permeabilities and thicknesses. The first case, $\delta = 0.74$ and $\sigma = 6.09$, is displayed in Fig. 4 (a) and (b) for the P_1 and P_2 data collection planes, and the second case, with $\delta = 1.37$ and $\sigma = 2.2$, is shown in Fig. 4(c) and (d) for the P_1 and P_2 data collection planes, respectively. A comparison of these figures reveals the significant influence of both the permeability parameter and the depth ratio on the flow behavior. As expected, for both cases, the

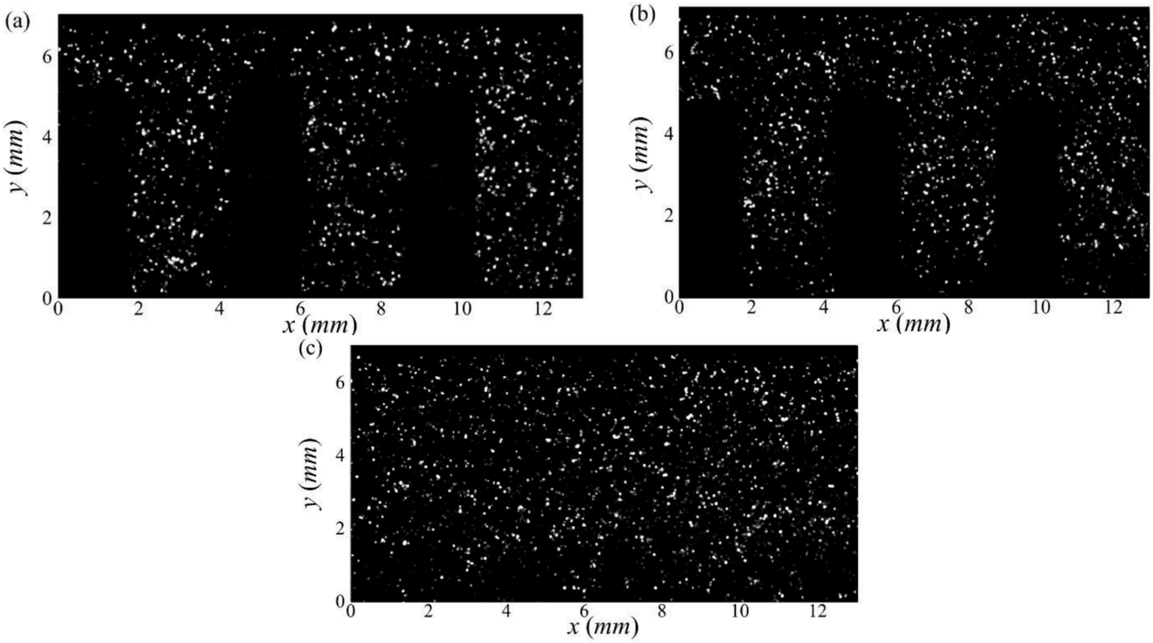

Fig. 3. The raw images of 1 % suspension with 1/8 large fluorescent particles for (a) the P_1 plane, (b) P_2 plane, and the (c) smooth channel. For a porous structure with the permeability parameter and depth ratio of with $\delta = 4.54$, $\sigma = 2.2$, respectively.

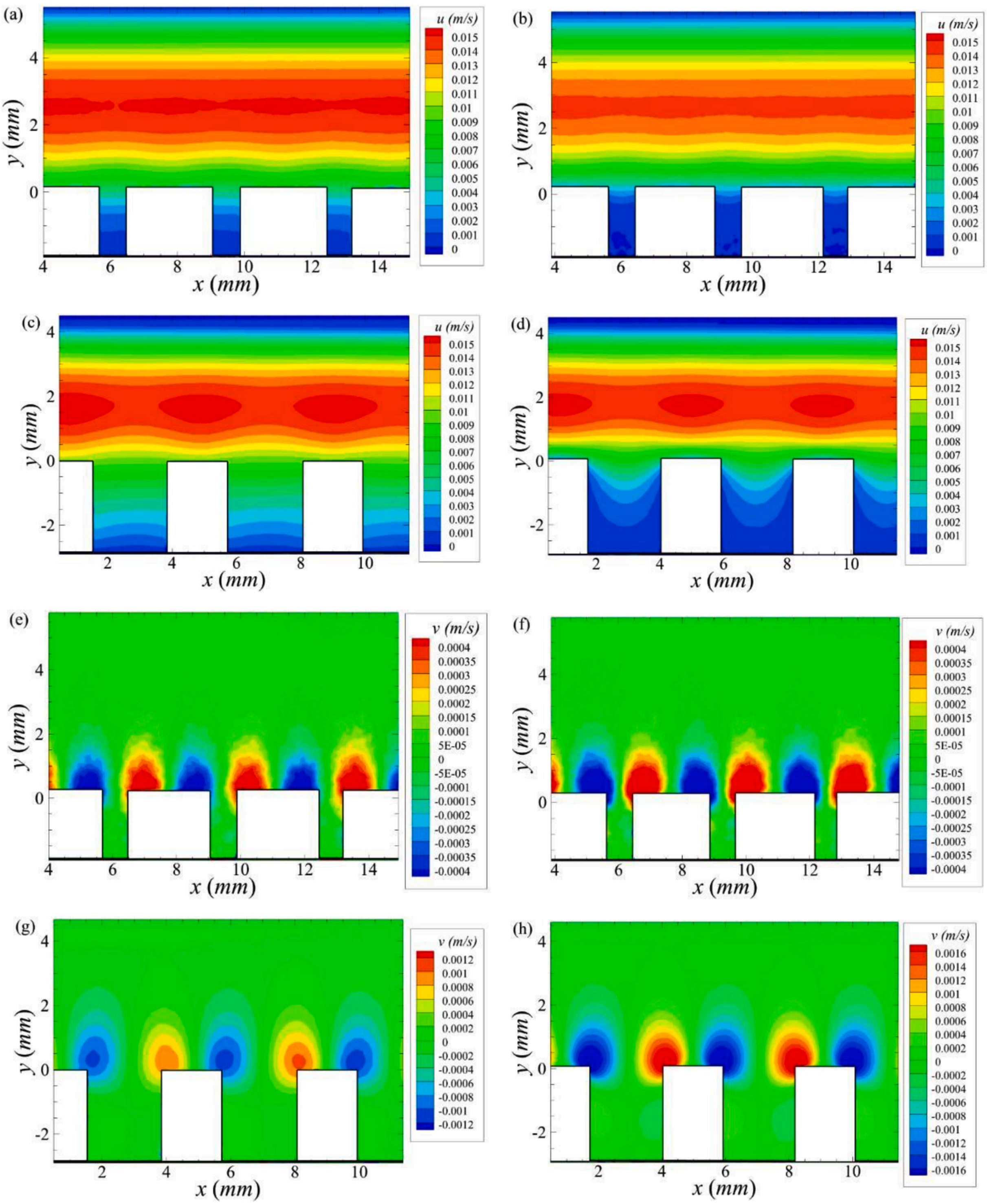

Fig. 4. The streamwise fluid velocity contours for 3 % suspension for within the (a) P_1 plane and (b) P_2 plane for the case of $\delta = 0.74$ and $\sigma = 6.09$. The u component of fluid velocity for the case $\delta = 1.37$ and $\sigma = 2.2$ within the (c) P_1 plane and (d) P_2 plane. The corresponding transverse fluid velocity contours for P_1 and P_2 planes: (e,f) $\delta = 0.74$ and $\sigma = 6.09$ and (g,h) $\delta = 1.37$ and $\sigma = 2.2$.

free-flow region resembles the Poiseuille flow profile. However, as the permeability decreases, the flow inside the porous structure becomes a plug flow and exhibits variations with height. The velocity peaks in the free-flow region also vary with the porous model thickness and physical properties. The velocity maxima are observed in the free-flow gaps over the rods, which is consistent with our previous findings (Haffner and Mirbod, 2020; Mirbod and Shapley, 2023) where the addition of particles resulted in velocity decay both in the free-flow region and over the porous structure. Fig. 4(e–h) depict the corresponding transverse velocity contours for these two cases in both the P_1 and P_2 data collection planes. It can be observed that the porous media with lower permeability exhibit lower magnitudes of the transverse velocity component (v-component). Moreover, an increase in porous permeability leads to a 34.6 % increase in the magnitude of the v-component from the P_1 plane to the P_2 plane.

To better understand the impact of the porous media properties on the flow structure in the presence of particles (i.e., 3 % suspension flow), we also calculated and plotted the average velocity profiles. The area average of the P_1 and P_2 planes was computed to represent the entire flow field (Arthur et al., 2009; Haffner and Mirbod, 2020). In the first series of experiments, we kept the thickness of the porous media constant while varying their porosity and permeability, corresponding to permeability parameters $\sigma = 6.09,\ \sigma = 3.46,\ \sigma = 2.2$. Fig. 5 displays the corresponding velocity profiles. In Fig. 5(a), it can be observed that as the permeability parameter decreases (indicating higher porous permeability), the location of the maximum velocity shifts towards the interface. For example, the porous media with $\sigma = 6.09$ has a maximum velocity at a dimensionless height of $\frac{Y}{L} = 0.9$, whereas for $\sigma = 2.2$, the maximum velocity occurs at $\frac{Y}{L} = 0.84$, representing a 7 % decrease in the $U_{\max}$ position along the profile. As expected, the velocity within the porous media decays as the porous permeability decreases. The shift in the maximum velocity is attributed to the resistance imposed by the rods in both Newtonian fluids and very dilute suspension flows. The velocity decays from the interfacial velocity to the so-called Darcy velocity, U_D (Haffner and Mirbod, 2020), then to zero at the lower wall boundary. This effect, as we have previously studied (Haffner and Mirbod, 2020), depends on both the thickness and physical properties of the porous structure. Moreover, as discussed earlier, it is evident that in diluted suspensions ($\phi_b \leq 0.1$) passing over and through the rods, the flow inside the free-flow region exhibits similar flow physics to that of the Newtonian suspending fluid, while the velocity decreases within the rods. In general, as the porous media thickness increases and its permeability decreases, the flow inside the porous media approaches a plug flow, which is a characteristic of flow inside porous media for Newtonian fluids. To investigate the impact of the depth ratio on the flow, velocity profiles were plotted for constant permeability parameters with varying depth ratios, as shown in Fig. 6. In Fig. 6(a), the velocity profiles for three different depth ratios are depicted at a constant permeability parameter $\sigma = 6.09$, which corresponds to the lowest permeability resulting in plug flow inside the porous structure. The graphs clearly demonstrate that increasing the thickness of the porous media leads to a shift in the location of the maximum velocity in the free flow region towards the interface. This shift is most pronounced in the case of the largest depth ratio, as shown in Fig. 6(b) and (c).

In our previous study (Haffner and Mirbod, 2020; Mirbod and Shapley, 2023), we extensively investigated how the concentration of the suspension (both very dilute, semi-dilute and concentrated suspensions) affects the flow field. In the current study, it was crucial to determine how the presence of suspension particles influences the flow over and through various porous media models. We then compared the averaged velocity profiles for a 3 % suspension to those of the pure solvent for one of the porous media models examined before, with a permeability parameter $\sigma = 2.2$ and a depth ratio $\delta = 4.54$. As depicted in Fig. 7, a clear agreement between the two profiles can be observed within the free-flow region. This agreement extends through the interface and the upper portion of the porous structure model. The trend of the profile within this region remains the same, but the velocity within the porous media is slightly lower for the 3 % suspension compared to the Newtonian solvent. However, a slight deviation appears in the profiles within the middle of the rods. The trend of the profile within this region remains the same, but the velocity within the porous media is slightly lower for the 3 % suspension compared to the Newtonian solvent. This suggests the presence of some intrinsic interaction between the suspension particles and the rods of the porous media. These findings align with those discussed in our earlier publication (Haffner and Mirbod, 2020).

3.2. Analysis of the interfacial parameters

To further investigate the effect of porous structures, we examined the properties at the interface, with a particular focus on the slip velocity and slip length. The slip velocity, defined as $U_S = U_{ave}\big|_{\frac{Y}{L}=0}$ (Haffner and Mirbod, 2020; Lauga and Stone, 2003), represents the most significant value at the interface. In Fig. 8(a), the slip velocity is normalized by the maximum area-averaged velocity in the free-flow region. This analysis allows for a comparison of the slip velocity with global parameters such as $U_{\max}$. From the results, it can be observed that increasing the permeability parameter σ leads to a decrease in the slip

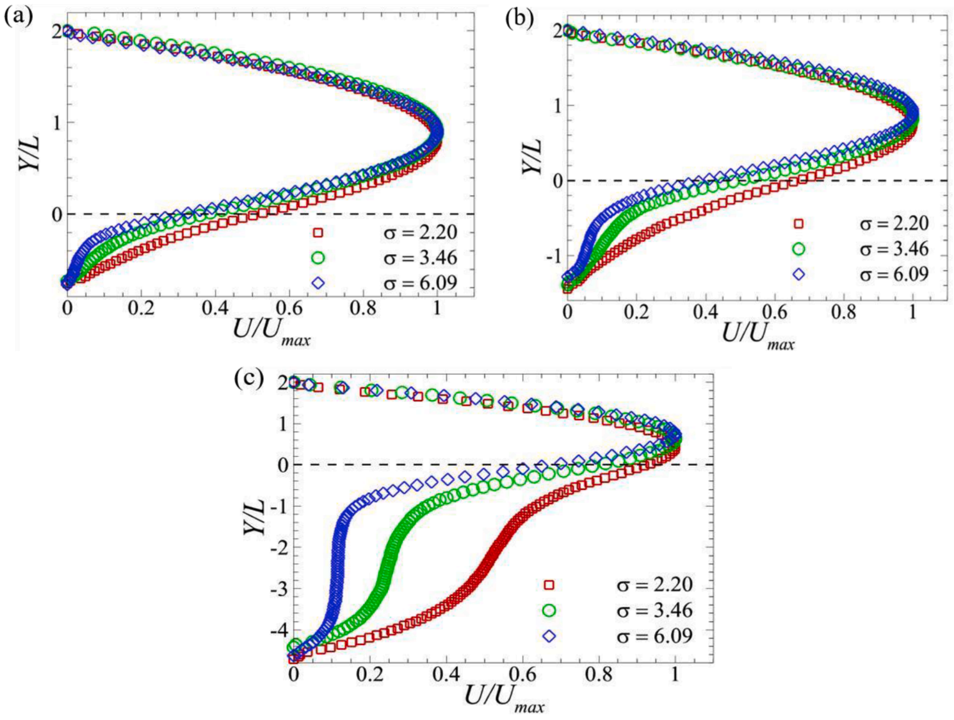

Fig. 5. The normalized fluid velocity profiles for a suspension particle volume fraction of $\phi_b = 3$ % and various permeability parameter: (a) $\delta = 0.74$, (b) $\delta = 1.37$, and (c) $\delta = 4.54$.

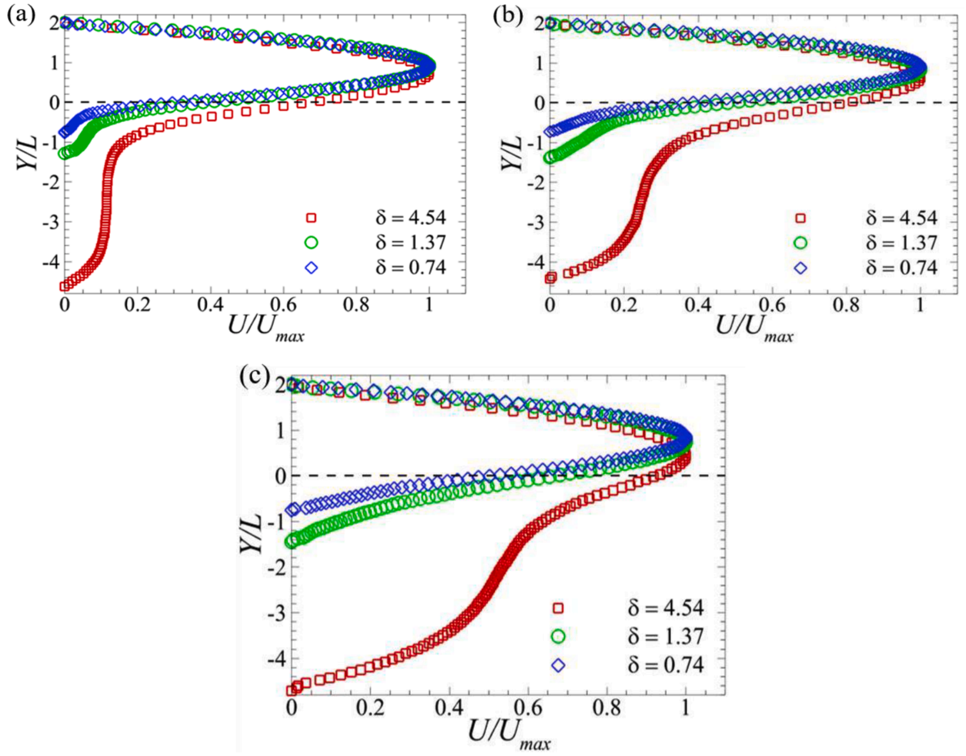

Fig. 6. The normalized fluid velocity profiles for a suspension particle volume fraction of $\phi_b = 3$ % and various porous permeability parameter: (a) $\sigma = 6.09$, (b) $\sigma = 3.46$, and (c) $\sigma = 2.2$.

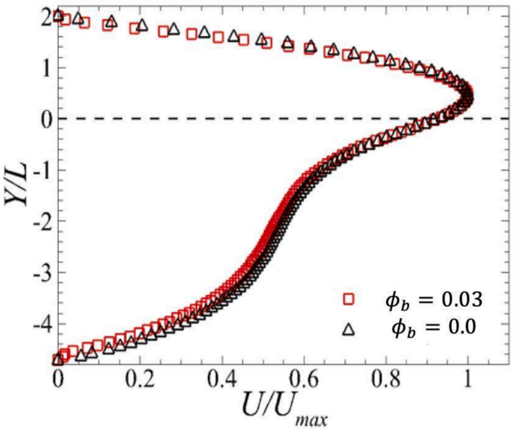

Fig. 7. The normalized fluid velocity profiles for a Newtonian solvent and the 3 % suspension over a porous media model with dimensionless properties of $\sigma = 2.2$ and $\delta = 4.54$.

velocity, while increasing the porous permeability results in an increase in the slip velocity. As both the porous thickness and permeability increase, the slip velocity gradually decreases, indicating that its magnitude approaches the maximum velocity in the free-flow region. This behavior aligns with the observations in the velocity profiles (see Figs. 5 and 6), where the maximum velocity shifted towards the interface. The dimensionless slip velocity has been previously investigated for Newtonian flow over various porous media models. Agelinchaab et al. (2006) examined flows over porous media with a depth ratio $\delta = 0.78$ and porosities ranging from 0.99 to 0.51, similar to the cases analyzed in our study. They reported a dimensionless slip velocity of approximately 1 (Agelinchaab et al., 2006). In our experiments, at the same depth ratio, we observed slightly larger values for the dimensionless slip velocity, ranging from 1.44 to 2.1. Agelinchaab et al. (2006) also investigated a depth ratio of $\delta = 2.55$, with porosities ranging from 0.99 to 0.51. The closest depth ratio in our experiments to their results is $\delta = 1.37$, where we found $1.65 \leq \frac{U_S}{\dot{\gamma}\sqrt{K}} \leq 2.74$. Comparatively, these values are still larger than what (Agelinchaab et al., 2006) reported. This discrepancy will be attributed to the presence of suspension particles in the flow. Beavers and Joseph (1967) examined Newtonian fluid flow over a porous media model with a porosity of 0.8, they reported dimensionless slip velocities ranging from 0.25 to 10 (Beavers and Joseph 1967). Gupte and Advani (1997) analyzed pure fluid flow over a glass fiber porous media, and they reported dimensionless slip velocities ranging from 2.3 to 14.3.

The shear rate is a significant parameter for characterizing the flow behavior in the presence of porous media models. At the interface, the shear rate is defined as $\dot{\gamma} = du/dy|_{y=0}$. In Fig. 8(b), we have normalized the shear rate with the bulk velocity and permeability. The results for the three depth ratios demonstrate that as the permeability parameter increases, the dimensionless shear rate also increases. For the depth ratio of 1.37, we observed a slight 0.3 % decrease in the dimensionless shear rate. We then analyzed the slip length, which is defined as the ratio between the velocity and the shear rate at the interface, i.e., $l_{slip} = \frac{U_S}{du/dy|_{y=0}}$ (Haffner and Mirbod, 2020). The slip length is shown in Fig. 8(c) and is dependent on both the σ and δ values. When the permeability of the porous structure decreases, the slip length decays. On the other hand, increasing the thickness of the rods tends to increase the slip length, except for the case of $\sigma = 6$. It is worth noting that the observed discrepancy in this case could be attributed to artifacts present in the suspension images.

These findings highlight the influence of the permeability parameter and depth ratio on the dimensionless shear rate and slip length, which are important factors for understanding the flow behavior near the interface between the fluid and porous media.

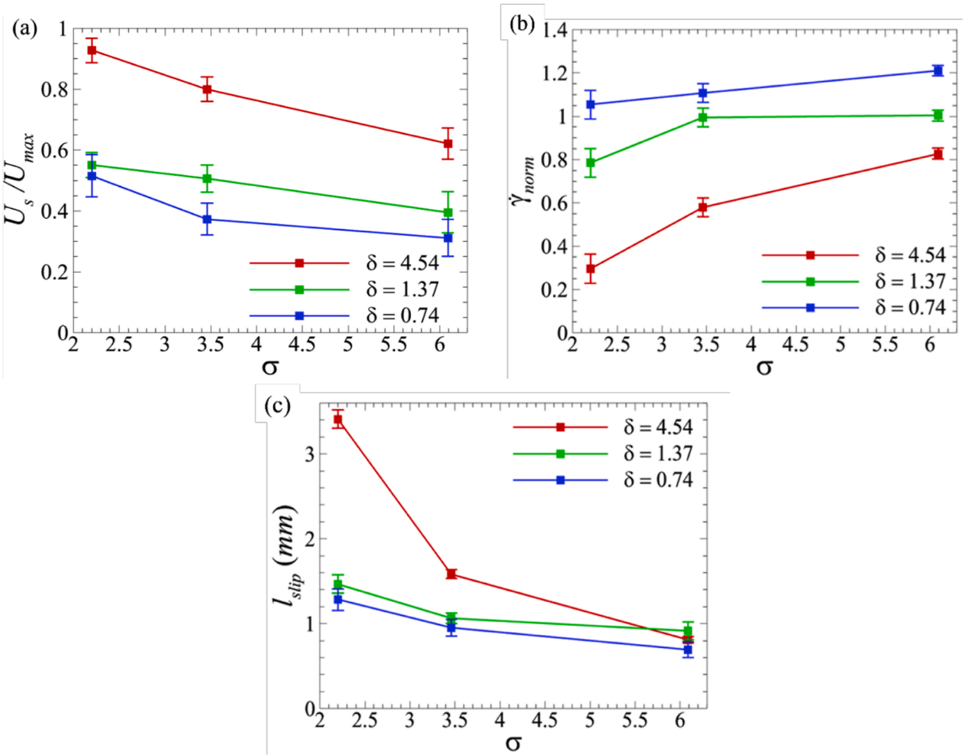

Fig. 8. (a) The averaged slip velocity normalized by the maximum area-averaged velocity for various test cases (with a maximum error of 13.4 %), (b) The dimensionless shear rate (with a maximum error of 6.7 %), and (c) the slip length (with an error of 9.4 %) evaluated at the interface. The error bars were calculated using the velocity uncertainties and methods outlined by Sciacchitano and Wieneke (2016) and Coleman and Steele (1995).

3.3. *Particle volume fractions*

To investigate the behavior of very dilute suspensions and the migration of particles within a channel with a porous structure model, we employed the OFTV technique to analyze particle concentration distributions. In the PIV experiments, the suspension particles had the same refractive index and density matched as the solvent. To visualize and track the suspension particles in the flow, we introduced fluorescent particles with the same density and diameter as the suspension particles. These fluorescent particles were illuminated within the laser sheet, allowing us to track a small portion of the suspension particles. For the particle distribution analysis, we kept the porous media model constant with properties of =2.2 and $\delta = 4.54$. The fluorescent particles had a particle solid volume fraction of 1/8 of $\phi_b = 1$ % (i.e., $\phi_0 = 0.12$ %). This concentration was maintained constant throughout the experiments to ensure clarity in the postprocessing of the images. Additionally, transparent PMMA particles were added to the suspension to achieve total bulk particle solid volume fractions of $\phi_b = 1$ %, 2 %, and 3 %.

Fig. 9 shows the track of fluorescent particles in the channel (Fig. 9 (a)) and the concentration maps for various very dilute suspension flows ($\phi_b = 1$ %, 2 %, and 3 %) at a volume flow rate of 70 ml/min. Although the flow is not fully developed over our field of view, we did not observe any significant evolution in the concentration distribution with axial distance *x*. In the concentration maps (Fig. 9(b)), several unique features can be observed in the porous media system. Firstly, it is evident that the particle concentration is enhanced both in the free-flow region and inside the rods of the porous structure. Furthermore, the concentration inside the porous structure is higher between the rods compared to on top of the rods. This nonuniform distribution indicates that particles migrate both inside and over the rods, moving from the channel edges towards the centerline of the rods due to the initial uniform distribution of particles. Therefore, the presence of rods in the porous structure alters the particle migration in the channel, causing particles to move away from the rods and sort between them, resulting in the maximum concentration in the free-flow region, at the center of the channel's height, and within the rods. Additionally, the concentration maps demonstrate that as the suspension bulk volume fractions increase, the particles tend to migrate away from the walls (high shear rate region) of the rods towards the rods' centerline (low shear rate region). In the free-flow region, the particles accumulate mainly on top of the rods. This behavior is like what is observed in a smooth channel flow at very low Reynolds numbers, where suspensions inside the rods tend to migrate to the lower shear rate region. However, the arrangement of rods in the porous structure leads to a distinct accumulation of particles within the free-flow region. Comparing these results with our recent work using MRI measurements for suspensions with higher volume fractions (Mirbod and Shapley, 2023), it was found that for concentrated suspensions, most of the particles flow through gaps between columns of rods. We observed banding occurred in a channel flow for higher concentrations (i.e., 20 %, 30 %, 40 %) using direct numerical simulations (DNSs) even in turbulent regime and when the particles do not penetrate in the porous region (Mirbod et al., 2023).

However, Fig. 9 demonstrates that even at very dilute suspensions, particles tend to flow around and through each rod in the porous structure, resulting in distinct particle migration over and through the porous structure. Therefore, the presence of a porous media model, such as the 3D structure used in this study, in the channel flow leads to particle migration to different locations. This might be due to the low resolution of the MRI compared to PIV and OFTV considered in this work. The streamwise average value of the particle volume fraction are shown in Fig. 10 for the P_1, P_2, and the averaged profiles for the $\phi_b = 1$ %, 2 %, and 3 % concentrated suspensions. The values for each case are normalized by the total count of the particles in the related FOV denoted by ϕ_0. While the error bars are not shown for clarity, the uncertainty (standard deviation) was consistent for each bulk volume fraction at an average value of 0.03. These graphs essentially counted the number of particles throughout the specified region between the rods and divided that by the total number of particles detected within the FOV. As can be

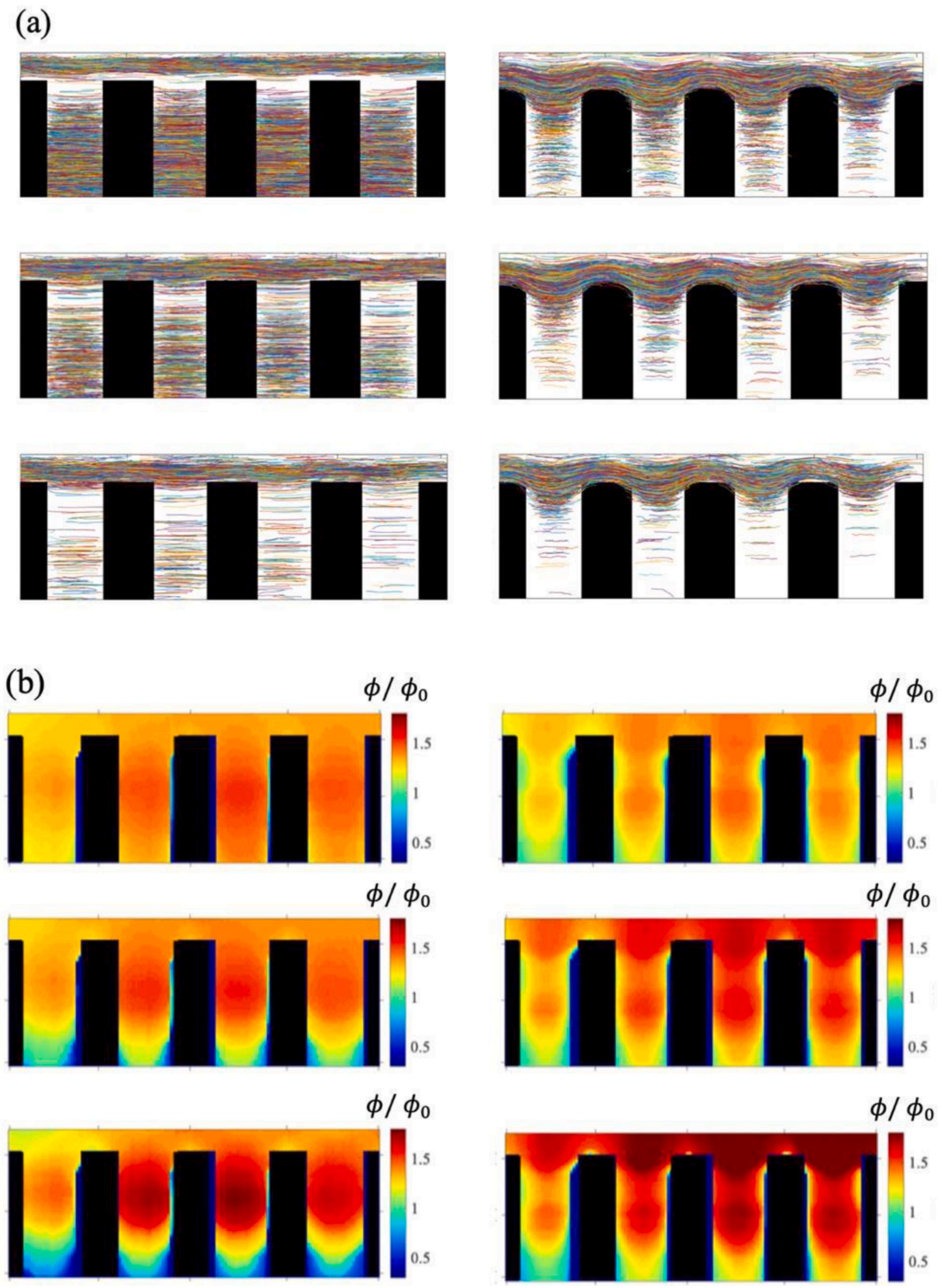

Fig. 9. (a) The particle trajectories for the P_1 (left column) and P_2 (right column) planes for the 1 % (top row), 2 % (middle row), and 3 % suspensions (bottom row) in x-y plane. (b) The normalized concentration contours for the P_1 (left column) and P_2 (right column) planes and $\phi_b = 1$ % (top row), $\phi_b = 2$ % (middle row), and $\phi_b = 3$ % suspension (bottom row). The porous model has $\sigma = 2.2$ and $\delta = 4.54$.

seen in Fig. 10(a), by increasing the bulk particle volume fractions in the P_1 plane, the particle migration inside the rods increases.

Fig. 10(b) demonstrates that the particle migration inside the rods is more pronounced in the P_2 plane compared to the P_1 plane for all three bulk volume fractions. This indicates that the flow properties and particle distribution are influenced by the porous structure model, and the particle migration behavior is more prominent in certain regions of the channel. The averaged profiles in Fig. 10(c) provide an overall representation of the particle volume fraction for different bulk volume fractions. The particle migration inside the rods increases with higher bulk volume fractions, showing that the effect of particle concentration is significant in determining the particle distribution within the porous media model. The results also suggest that higher bulk volume fractions lead to increased particle migration inside the rods of the porous structure.

The peak of the particles near the interface and inside the rods is also

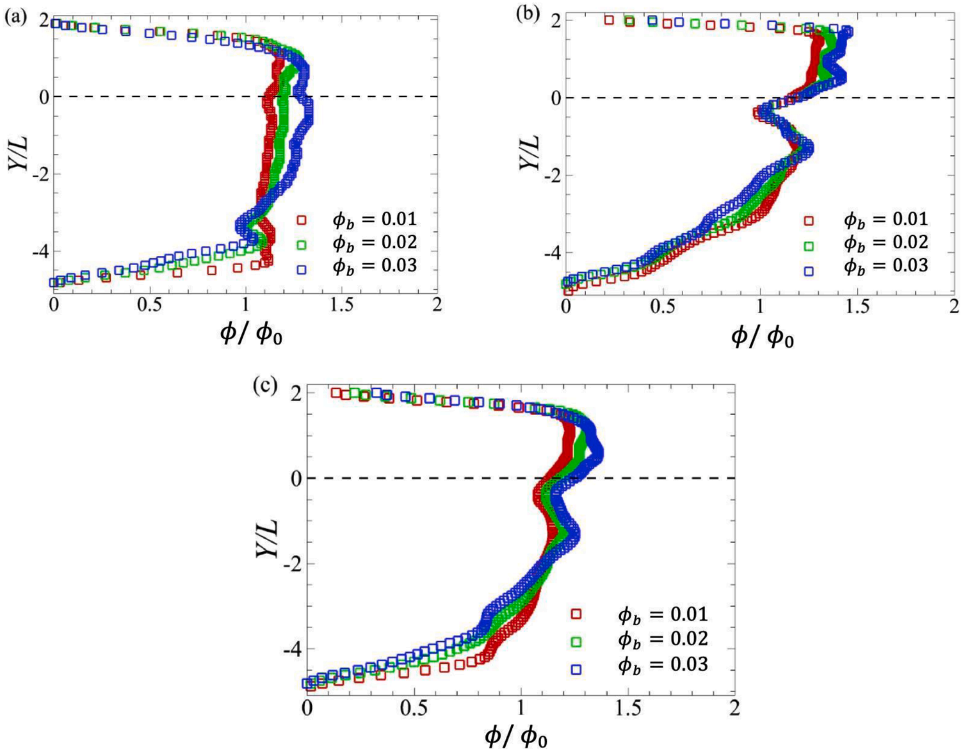

Fig. 10. Probability density functions (PDFs) for the (a) P_1, (b) P_2 and (c) the average of the two for the three different concentrations $\phi_b = 1$ %, $\phi_b = 2$ %, and $\phi_b = 3$ % examined in this study.

more apparent, while the particles distribute almost uniformly inside the rods for very low particle volume fractions. In the P_2 plane, shown in Fig. 10(b), however, we notice a layering in the flow. There is a peak value of dense particles in both free flow region and inside the porous layer for all concentrations. Fig. 10(c) (the average of the P_1 and P_1 planes) clearly shows that the layering becomes stronger by increasing the bulk volume fraction. While the maximum concentration occurs inside the free flow region, there is another maximum inside the porous layer due to particle migration inside the rods. Previous works, in smooth channels for both semi-dilute and dense suspensions, observed that particle migration occurs from the high shear rate region to the lower shear rate region (Morris, 2020; Lyon and Leal, 1998a; Leighton and Acrivos, 1987; Phillips et al., 1992; Mirbod, 2016; Guazzelli and Pouliquen, 2018; Guazzelli and Morris, 2011; Lyon and Leal, 1998b) known as shear-induced migration, with a rich history of research that is explained in several papers (Guazzelli and Morris, 2011; Guazzelli and Pouliquen, 2018). Herein, we showed that at very low Reynolds number, the wall structure plays a critical role that impact both the velocity and concentration of particles in the channel. We also observe that regions of high particle volume fraction and low shear rate magnitude, particularly in the free-flow region, are coincide and the particle concentration profiles are maximum at the channel centerline and inside the rods. For instance, as can be observed in Fig. 7, inside the free-flow region where the velocity is maximum near the interface, the concentration is lower, while it is higher in the channel mid-center and inside the rods. This effect then reduces on top of the rods and near the edges of the channel forming particle banding.

4. Conclusions

This study delved into the characterization of a non-Brownian, non-colloidal suspension containing rigid, spherical micron-sized particles within a partially filled channel featuring diverse porous media models configurations. These media comprised square arrays of rods oriented perpendicular to the flow direction. By examining three permeabilities ($K = 1.12 \times 10^3$ cm^2, 3.42×10^{-3} cm^2, and 7.92×10^3 cm^2), porosities ($\varepsilon = 0.7, 0.8,$ and 0.9), and three different porous media thicknesses ($H = 0.2$ cm, 0.3 cm, and 0.5 cm), we aimed to elucidate the complex interactions governing the system's behavior. While Particle Image Velocimetry (PIV) provided velocity data, the OFTV technique was harnessed to assess particle volume fractions for a specific porous media model ($H = 0.5$ cm and $K = 7.92 \times 10^3$ cm^2) across varying bulk suspension concentrations (1 % to 3 %). Our observations unveiled compelling insights. For the highest depth ratio ($\delta = \frac{H}{L} = 4.54$), the flow exhibited periodic patterns further upstream compared to lower permeabilities, resulting in fully developed flow velocity profiles. The interplay of depth ratio and permeability exerted significant influence on the location of periodic flow behavior. Across all examined porous media models, clear parabolic velocity profiles emerged within the free flow regions. Remarkably, the location of maximum velocity along these profiles shifted based on porous media properties. We found that the slip velocity normalized by $U_{\max}$ diminished as porous permeability decreased.

Further employing OFTV in the context of $\delta = 4.54$ and $\sigma = \frac{L}{\sqrt{K}} = 2.2$, with 1 %, 2 %, and 3 % suspensions, we revealed a pivotal role of channel wall structure in particle migration during low Reynolds regimes. Even small particle additions to the flow, when interacting with a 3D porous structure comprising a square array of rods on its lower surface, led to particle migration away from the rods. This phenomenon manifested both within the rods and the free flow region, inducing non-uniform particle distributions. As suspension concentration increased, interactions between particles, rods, and walls instigated changes in velocity and concentration profiles. Nonuniform particle distribution stemming from shear-induced migration was observed over and within the porous model. Enhanced particle concentration led to reduced velocity through the porous region. The arrangement and structure of the rods played a critical role; accumulation between rods occurred due to the lower shear rate in axial planes between rods compared to the axial planes on top. The surface structure resulted in particle migration, particularly evident in banding effects near the free flow and porous regions upon higher particle addition. This impact hinged on multiple parameters including suspension properties, particle size and shape, and the porous structure thickness and properties.

Future directions include varying porous medium parameters and employing advanced 3D measurement techniques such as Shake-the-box systems to further examine particle migration, leading to an improved understanding of heterogeneous concentration fields and modified velocity profiles. This data holds potential for 1) further investigating the impact of both particles and structured surfaces in the flow using discrete-particle simulations, 2) refining continuum models such as diffusive flux model (DFM) and suspension balance model (SBM) to capture the particle migration over and through structured surfaces, and 3) advancing analyses involving particle interactions within structured surfaces and porous media.

CRediT authorship contribution statement

Eileen A. Haffner: Writing – original draft, Visualization, Validation, Software, Resources, Project administration, Methodology, Investigation, Formal analysis, Data curation. **Theresa Wilkie:** Software, Formal analysis, Data curation. **Jonathan E. Higham:** Writing – review & editing, Writing – original draft, Visualization, Validation, Software, Resources, Methodology, Investigation, Formal analysis, Data curation. **Parisa Mirbod:** Writing – review & editing, Writing – original draft, Visualization, Validation, Supervision, Software, Resources, Project administration, Methodology, Investigation, Funding acquisition, Formal analysis, Data curation, Conceptualization.

Declaration of competing interest

The authors declare the following financial interests/personal relationships which may be considered as potential competing interests:

Parisa Mirbod reports financial support was provided by University of Illinois Chicago. Parisa Mirbod reports a relationship with University of Illinois Chicago that includes: employment. If there are other authors, they declare that they have no known competing financial interests or personal relationships that could have appeared to influence the work reported in this paper.

Data availability

Data will be made available on request.

Acknowledgments

This work has been supported partially by National Science Foundation Award no. 1854376 and partially by Army Research Office Award no. W911NF-18-1-0356 to P.M. and E.A.H. T.W. was also an undergraduate student supported by National Science Foundation Award no. 1854376 as part of this project.

References

Adrian, R.J. and Westerweel, J., "Particle Image Velocimetry,"30 (2011). 10.1017/S0001924000006734.

Agelinchaab, M., Tachie, M.F., Ruth, D.W., 2006. Velocity measurement of flow through a model three-dimensional porous medium. Physics of Fluids 18 (1), 017105–017111. https://doi.org/10.1063/1.2164847.

Arthur, J., 2019. Experimental investigation of porous medium structural effects on a coupled porous media-free zone laminar flow. SN Appl. Sci 1 (9), 1–13. https://doi.org/10.1007/s42452-019-1070-7.

Arthur, J.K., Ruth, D.W., Tachie, M.F., 2009. PIV measurements of flow through a model porous medium with varying boundary conditions. Journal of Fluid Mechanics 629, 343–374. https://doi.org/10.1017/S0022112009006405.

Averbakh, A., Shauly, A., Nir, A., Semiat, R., 1997. Slow viscous flows of highly concentrated suspensions - Part I: Laser-Doppler velocimetry in rectangular ducts. Int. J. Multiphase Flow 23, 409–424. https://doi.org/10.1016/S0301-9322(96)00078-X.

Barnes, Howard A. Dispersion rheology 1980: a survey of industrial problems and academic progress. Process Technology Group of the Royal Chemical Society, 1981. 10.1016/0377-0257(82)85024-6.

Beavers, G.S., Joseph, D.D., 1967. Boundary conditions at a naturally permeable wall. Journal of Fluid Mechanics 30, 197–207. https://doi.org/10.1017/S0022112067001375.

Bernal, J.D., Mason, J, 1960. Packing of spheres: co-ordination of randomly packed spheres. Nature 188 (4754), 910–911. https://doi.org/10.1038/188910a0.

Coleman, H.W., Steele, W.G., 1995. Engineering application of experimental uncertainty analysis. AIAA Journal 33 (10), 1888–1896. https://doi.org/10.2514/3.12742.

Desmond, Kenneth W., Weeks, Eric R., 2014. Influence of particle size distribution on random close packing of spheres. Physical Review E 90 (2), 022204. https://doi.org/10.1103/physreve.90.022204.

Frank, M., Anderson, D., Weeks, E.R., Morris, J.F., 2003. Particle migration in pressure-driven flow of a Brownian suspension. Journal of Fluid Mechanics 493, 363–378. https://doi.org/10.1017/S0022112003006001.

Guazzelli, E. and Morris, J.F., "A physical introduction to suspension dynamics," 45 (2011). 10.1017/CBO9780511894671.

Guazzelli, É, Pouliquen, O., 2018. Rheology of dense granular suspensions. J. Fluid Mech. 852 https://doi.org/10.1017/jfm.2018.548.

Gupte, S.K., Advani, S.G., 1997. Flow near the permeable boundary of a porous medium: An experimental investigation using LDA. Experiments in Fluids 22 (5), 408–422. https://doi.org/10.1007/s003480050067.

Haffner, E.A., Bagheri, M., Higham, J.E., Cooper, L., Rowan, S., Stanford, C., Mashayek, F., Mirbod, P., 2021. An experimental approach to analyze aerosol and splatter formations due to a dental procedure. Exp Fluids 62 (10). https://doi.org/10.1007/s00348-021-03289-2, 202.

Haffner, E.A., Mirbod, P., 2020. Velocity measurements of dilute particulate suspension over and through a porous medium model. Physics of fluids 32 (8), 83608. https://doi.org/10.1063/5.0015207.

Hall, M.J., Hiatt, J.P., 1994. Exit flows from highly porous media. Physics of Fluids 6 (2), 469–479. https://doi.org/10.1063/1.868344.

Hampton, R.E., Mammoli, A.A., Graham, A.L., Tetlow, N., Altobelli, S.A., 1997. Migration of particles undergoing pressure-driven flow in a circular conduit. Journal of Rheology 41 (3), 621–640. https://doi.org/10.1122/1.550863.

Dreesen F., Hinsch H., Hinrichs H., Hinsch K., Roshop A. 1993. "Holographic and stereoscopic advances in 3-D PIV", ASME-PUBLICATIONS-FED,148:33-33.10.1007/978-3-642-84824-7_147.

James, D.F., Davis, A.M.J., 2001. Flow at the interface of a model fibrous porous medium. Journal of Fluid Mechanics 426, 47–72. https://doi.org/10.1017/S0022112000002160.

Jana, S.C., Kapoor, B., Acrivos, A., 1995. Apparent wall slip velocity coefficients in concentrated suspensions of noncolloidal particles. Journal of Rheology 39 (6), 1123–1132. https://doi.org/10.1122/1.550631.

Jesinghausen, S., Weiffen, R., Schmid, H., 2016. Direct measurement of wall slip and slip layer thickness of non-Brownian hard-sphere suspensions in rectangular channel flows. Exp Fluids 57 (9), 1–15. https://link.springer.com/article/10.1007/s00348-016-2241.

Johnston, W., Dybbs, A. and Edwards, R., "Measurement of fluid velocity inside porous media with a laser anemometer," The Physics of fluids, 18.7, (1975), 913-914. 10.1063/1.861229.

Kapoor, B., Acrivos, A., 1995. Sedimentation and sediment flow in settling tanks with inclined walls. Journal of Fluid Mechanics 290, 39–66. https://doi.org/10.1017/S0022112095002412.

Koh, C.J., Hookham, P., Leal, L.G., 1994. An experimental investigation of concentrated suspension flows in a rectangular channel. Journal of Fluid Mechanics 266, 1–32. https://doi.org/10.1017/S0022112094000911.

Krieger, Irvin M., 1972. Rheology of monodisperse latices. Advances in colloid and interface science 3, 111–136. https://doi.org/10.1016/0001-8686(72)80001-0.

Larson, R.G., '"The structure and rheology of complex fluids," (1999). 10.1515/arh-2000-0024.

Lauga, E., Stone, H.A., 2003. Effective slip in pressure-driven Stokes flow. Journal of Fluid Mechanics 489, 55–77. https://doi.org/10.1017/S0022112003004695.

Leighton, D., Acrivos, A., 1987. The shear-induced migration of particles in concentrated suspensions. Journal of Fluid Mechanics 181 (1), 415–439. https://doi.org/10.1017/S0022112087002155.

Lyon, M.K., Leal, L.G., 1998. An experimental study of the motion of concentrated suspensions in two-dimensional channel flow. Part 1. Monodisperse systems. Journal of Fluid Mechanics 363, 25–56. https://doi.org/10.1017/S0022112098008817.

Lyon, M.K., Leal, L.G., 1998. An experimental study of the motion of concentrated suspensions in two-dimensional channel flow. Part 2. Bidisperse systems. Journal of Fluid Mechanics 363, 57–77. https://doi.org/10.1017/S0022112098008829.

Miller, R.M., Morris, J.F., 2006. Normal stress-driven migration and axial development in pressure-driven flow of concentrated suspensions. Journal of Non-Newtonian Fluid Mechanics 135 (2), 149–165. https://doi.org/10.1016/j.jnnfm.2005.11.009.

Mirbod, P., Haffner, E.A., Bagheri, M., Higham, J., 2021. Aerosol formation due to a dental procedure: insights leading to the transmission of diseases to the environments. Journal of The Royal Society Interface. https://doi.org/10.1098/rsif.2020.0967.

Mirbod, Parisa., 2016. Two-dimensional computational fluid dynamical investigation of particle migration in rotating eccentric cylinders using suspension balance model. International Journal of Multiphase Flow 80, 79–88. https://doi.org/10.1016/j.ijmultiphaseflow.2015.11.002.

Mirbod, P., Abtahi, S.M., Bilondi, A.M., Rosti, E.M., Brandt, L., 2023. Turbulent channel flow of suspensions of neutrally buoyant particles over porous media. Journal of Fluid Mechanics 954, A8. https://doi.org/10.1017/jfm.2022.982.

Mirbod, P., Shapley, N.C., 2023. Particle migration of suspensions in a pressure-driven flow over and through a porous structure. Journal of Rheology 67, 417–432. https://doi.org/10.1122/8.0000505.

Miura, K., Itano, T., Sugihara-Seki, M., 2014. Inertial migration of neutrally buoyant spheres in a pressure-driven flow through square channels. Journal of fluid mechanics 749, 320–330. https://doi.org/10.1017/jfm.2014.232.

Morris, J.F., 2020. Toward a fluid mechanics of suspensions. Phys. Rev. Fluids 5 (11). https://doi.org/10.1103/PhysRevFluids.5.110519.

Nott, P.R., Brady, J.F., 1994. Pressure-driven flow of suspensions: simulation and theory. Journal of Fluid Mechanics 275, 157–199. https://doi.org/10.1017/S0022112094002326.

Patil, V.A., Liburdy, J.A., 2013. Flow characterization using PIV measurements in a low aspect ratio randomly packed porous bed. Exp Fluids 54 (4), 14901–14919. https://doi.org/10.1007/S00348-013-1497-3.

Peurrung, L.M., Rashidi, M., Kulp, T.J., 1995. Measurement of porous medium velocity fields and their volumetric averaging characteristics using particle tracking velocimetry. Chemical Engineering Science 50 (14), 2243–2253. https://doi.org/10.1016/0009-2509(94)00509-P.

Phillips, R.J., Armstrong, R.C., Brown, R.A., Graham, A.L., Abbott, J.R., 1992. A constitutive equation for concentrated suspensions that accounts for shear-induced particle migration. Physics of Fluids A: Fluid Dynamics 4 (30), 30–40. https://doi.org/10.1063/1.858498.

Raffel, M., Willert, C.E., Wereley, S.T. and Kompenhas, J., “Particle image velocimetry: a practical guide,"2 (2007). 10.1007/978-3-540-72308-0.

Ramesh, P., Bharadwaj, S., Alam, M., 2019. Suspension Taylor-Couette flow: co-existence of stationary and travelling waves, and the characteristics of Taylor vortices and spirals. Journal of Fluid Mechanics 870, 901–940. https://doi.org/10.1017/jfm.2019.291.

Roberts, B.W., Olbricht, W.L., 2006. The distribution of freely suspended particles at microfluidic bifurcations. AIChE Journal 52 (1), 199–206. https://doi.org/10.1002/AIC.10613.

Sciacchitano, A., Wieneke, B., 2016. PIV uncertainty propagation. Measurement Science and Technology 27 (8), 084006. https://doi.org/10.1088/0957-0233/27/8/084006.

Semwogerere, D., Morris, J.F., Weeks, E.R., 2007. Development of particle migration in pressure-driven flow of a Brownian suspension. Journal of Fluid Mechanics 581, 437–451. https://doi.org/10.1017/S0022112007006088.

Singh, A., Nir, A., Semiat, R., 2006. Free-surface flow of concentrated suspensions. International Journal of Multiphase Flow 32 (7), 775–790. https://doi.org/10.1016/j.ijmultiphaseflow.2006.02.018.

Sinton, S.W., Chow, A.W., 1991. NMR flow imaging of fluids and solid suspensions in Poiseuille flow. Journal of Rheology 35 (5), 735–772. https://doi.org/10.1122/1.550253.

Sohn, H.Y, c, Moreland, 1968. The effect of particle size distribution on packing Density. The Canadian Journal of Chemical Engineering 46, 162–167. https://doi.org/10.1002/cjce.5450460305.

Tamayol, A., Bahrami, M., 2011. Transverse permeability of fibrous porous media. Physical review. E, Statistical, nonlinear, and soft matter physics, 046314. https://doi.org/10.1103/PhysRevE.83.046314, 83.4 Pt 2.

Tripathi, Anubhav, Acrivos, Andreas, 1999. Viscous resuspension in a bidensity suspension. International Journal of Multiphase Flow 25, 1–14. https://doi.org/10.1016/S0301-9322(98)00036-6.

Van Dinther, A., Schroën, C., Vergeldt, F.J., Van der Sman, R., Boom, R.M., 2012. Suspension flow in microfluidic devices—A review of experimental techniques focussing on concentration and velocity gradients. Adv.Colloid Interface Sci 173, 23–34. https://doi.org/10.1016/j.cis.2012.02.003.

Westerweel, J., Elsinga, G.E., Adrian, R.J, 2013. Particle image velocimetry for complex and turbulent flows. Annual Review of Fluid Mechanics 45, 409–436. https://doi.org/10.1146/annurev-fluid-120710-101204.

Wiederseiner, S., Andreini, N., Epely-Chauvin, G., Ancey, C., 2011. Refractive-index and density matching in concentrated particle suspensions: a review. Exp Fluids 50 (5), 1183–1206. https://doi.org/10.1007/S00348-010-0996-8.

Xi, C., Shapley, N.C., 2008. Flows of concentrated suspensions through an asymmetric bifurcation. Journal of Rheology 52 (2), 625–647. https://doi.org/10.1122/1.2833469.

Zade, S., Costa, P., Fornari, W., Lundell, F., Brandt, L., 2018. Experimental investigation of turbulent suspensions of spherical particles in a square duct. Journal of fluid mechanics 857, 748–783. https://doi.org/10.1017/jfm.2018.783.